MODELING MARCI AND TES APHELION CLOUD BELT OPTICAL DEPTH PEAK DIFFERENCES WITH THE AMES MGCM.

D. R. Klassen, *Rowan University, New Jersey, USA (klassen@rowan.edu)*, **M. A. Kahre,** *NASA Ames Research Center, California, USA*, **M. J. Wolff,** *Space Science Institute, Colorado, USA*, **R. M. Haberle, J. L. Hollingsworth,** *NASA Ames Research Center, California, USA*.

Introduction: The martian aphelion cloud belt (ACB) is a well-studied phenomenon; its seasonal morphology and typical optical depths were, in part, characterized by HST violet images and microwave observations (e.g., James et al., 1996; Clancy et al., 1996; Wolff et al., 1999). Follow up, long-term studies by orbiting instruments (e.g., Pearl et al., 2001; Smith et al., 2003; Smith, 2004) characterized the growth and decline of the ACB as well as a baseline set of zonally averaged optical depths as a function of latitude and season. All this work provided ground-truth for the assessment and modification of Mars general circulation models (GCMs) and current models provide good agreement with observations (e.g., Montmessin et al., 2004; Haberle et al., 2010), although there are still improvements to be made.

Figure 1 (from Kahre et al., 2017) shows that the Ames GCM predicts ACB cloud optical depths that are too low in the infrared (IR) and too high in the ultraviolet (UV) when compared to Mars Global Surveyor (MGS) Thermal Emission Spectrometer (TES) and Mars Reconnaissance Orbiter (MRO) Mars Color Imager (MARCI), respectively. The observations also show a shift of about 10–15° of L_S between the two that is not replicated in the GCM output.

Looking at the ratio of the MARCI-TES UV-to-IR optical depths there is a distinct upward trend from $L_S = 30°$–$120°$ as the ACB grows through the season. Figure 2 shows plots of the cloud particle efficiency coefficients for extinction in the UV and both extinction and absorption in the IR (top panel). When we ratio the trends (bottom panel) we see very high values for small particles and decreasing rapidly as the particle size increase. Since optical depth is a direct function of the efficiency coefficient, the upward trend in the observed optical depth ratio in Figure 1 implies an evolution to smaller particles in the ACB as the season progresses. This trend is not seen in the GCM output; in fact the differences in optical depths between it and the observations implies the cloud particle sizes are too small overall.

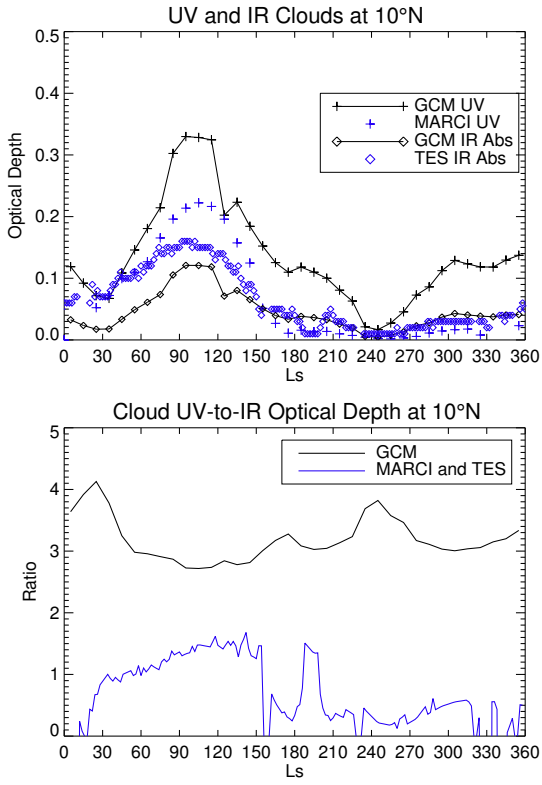

Figure 1: Top—GCM zonal average cloud optical depths compared to observations from TES and MARCI as a function of L_S. Bottom—GCM UV-to-IR ratio of zonal cloud optical depth and MARCI-to-TES ratio.

Investigations We used the Ames Mars GCM v.2.3 as described in Kahre et al. (2017) in a simplified form in order to test the effect on cloud particle size by changes in dust number density. The simple idea is that if the dust number density is increased there will be more cloud nucleation sites competing for the same water vapor

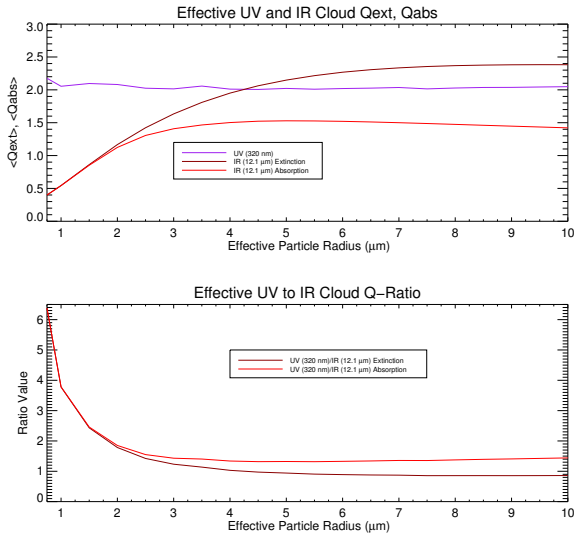

Figure 2: Top—Cloud particle efficiency coefficients in the UV and IR as a function of particle effective radius. Bottom—The ratio of UV to the two IR efficiency coefficients above. There is a distinct trend allowing the ratio value to imply the effective radius of the particles.

amount leading to smaller cloud particles. Conversely, if the dust number density is reduced there will be fewer nucleation sites and thus larger cloud particles. In order to be sure we are only looking at the effects of the dust as nucleation sites alone, we ran the GCM in a mode that calculates dust radiative effects from a fixed, TES-based dust optical depth value and not the transported dust being used as nucleation sites. Additionally, the radiative effects of the clouds themselves were turned completely off.

Transported dust comes from the surface and is forced to attempt to match the TES observed values—if at any time or place it is too low, more dust is injected into the lowest atmosphere layer and allowed to be transported by the model winds. In order to test the effects of more or less dust, the entire TES map was scaled by factors of $\times 3$ and $\times 1/2$—that is, the reference map of dust optical depth was adjusted and the model matching routine would attempt to match the new values. The model was allowed to run for two full mars-years in order to equilibrate and results from the model year three were extracted.

Results As can be seen in Figure 3, changing the dust optical depth reference map changes the number density of dust and cloud particles as expected. When the dust is increased, there are more nucleation sites and thus more cloud particles and when the dust is decreased there are fewer dust particles and thus fewer cloud particles. In order to investigate the sizes of the cloud particles

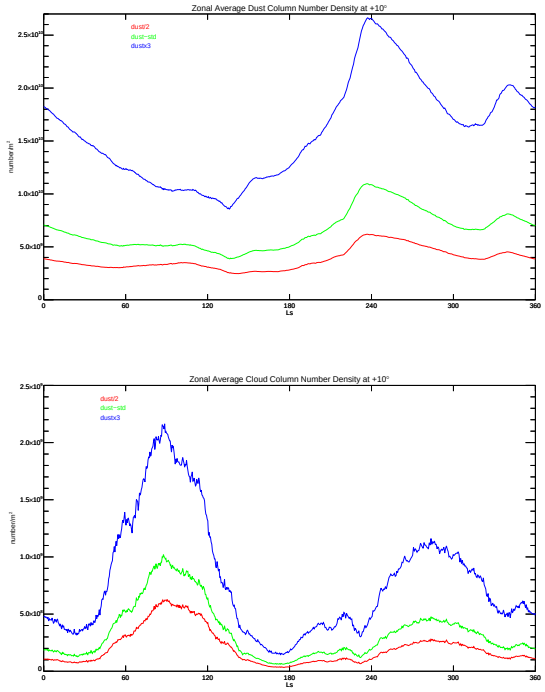

Figure 3: The dust (top) and cloud (bottom) number density, zonally averaged, at 10°N for three versions of dust reference: TES reference map $\times 1/2$, standard, and $\times 3$.

we relied on the fact that the model uses a log-normal particle size distribution which allows us to create a relationship between the total mass of cloud particles per model cell, the total number of cloud particles, and the effective radius of those particles.

By definition of a log-normal size distribution we know that the number of particles n at the particular radius, r is given by:

$$n(r)\,dr = \frac{1}{r\sigma_0\sqrt{2\pi}} \exp\left[\frac{1}{2}\left(\frac{ln(r/R_0)^2}{\sigma_0}\right)\right] dr$$

where σ_0 is the distribution width and R_0 is the median radius. The total mass of particles, M_0 is then:

$$M_0 = \frac{4}{3}\pi\rho \int r^3 n(r)\,dr = \frac{4}{3}\pi\rho N_0 R_0^3 \exp(9\sigma_0^2/2)$$

where ρ is the mass-density of the individual particles, and N_0 is the total number of cloud particles. Solving this for R_0 gives:

$$R_0 = \left[\frac{3M_0}{4\pi\rho N_0}\right]^{1/3} \exp(-3\sigma_0^2/2)$$

Taking further advantage of the properties of log-normal distributions we can find the effective radius, R_{eff}, from:

$$R_{\text{eff}} = R_0 \exp(5\sigma_0^2/2)$$

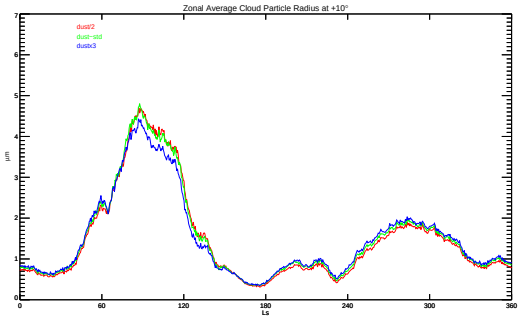

Figure 4: The column and zonally averaged cloud particle effective radius at 10°N for three versions of dust reference: TES reference map $\times 1/2$, standard, and $\times 3$.

The effective radius is a cross-section-area weighted average radius of the distribution and as such represents the single particle size that can represent the entire distribution in terms of the efficiency coefficients for the calculation of optical depth.

Putting all this together we can retrieve from the GCM output the values of M_0 and N_0 for every model cell and calculate R_{eff} from them. These can then be column and zonally averaged over time. Note that because R_{eff} has a $1/N_0$ dependance, areas that have few to zero particles in them will have large, unphysical radii that will dominate these averages, therefore we weight R_{eff} in each cell by its corresponding N_0 for the average. De-weighting is done by simply dividing back out a global-temporal single average value of N_0. The technique appears to give the best results.

The graph of these averaged effective radius values for all three model runs are presented in Figure 4. Surprisingly there is very little change in the effective radius between the three model runs—although the small changes are in the correct direction. The higher dust model does have smaller cloud particles and the lower dust model does have larger cloud particles. However, all the models hover around $R_{\text{eff}} = 4.75$ μm at the peak—much larger than the implied 1–2 μm implied by the MARCI-TES UV-to-IR ratio slope seen in Figure 1.

The model using the $\times 1/2$ reference dust optical depth map effective radii, which have larger cloud particles than the standard, are used to calculate the column optical depth which is then zonally averaged; the results are in Figure 5. As can be seen, this change does nothing to create a shift in peak optical depth between the two wavelength bands. While the optical depth values in the IR are much closer to the observed TES values (Figure 1) the UV values are still to high by about a factor of two in the peak.

Conclusions The above tests indicate that the differences between the GCM model output optical depths

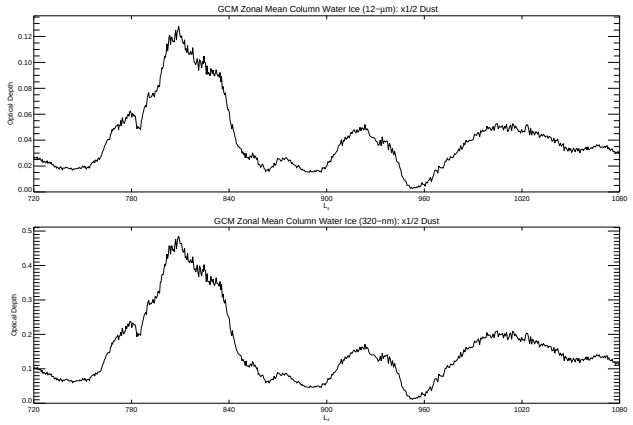

Figure 5: Calculated zonally averaged optical depth for the TES dust reference map $\times 1/2$ (larger cloud particles) model run in the IR (top) and UV (bottom).

and the observed optical depths are not due simply to an overall change in cloud particle seed nuclei. Additional tests were run by using the standard dust reference optical depth map but then switching to the higher/lower reference map for only the summer season but with no significant change in the results—strengthening our conclusion.

The next logical step would be to add in more sophistication to the model. We could make the transported dust radiatively active instead of using the constant TES dust map for that and even make the clouds themselves radiatively active. Models could then be run with varying the amount of dust universally or seasonally.

New Direction for Presentation It needs to be noted that the optical depths being plotted from the GCM are those computed over relatively broad spectral bands in order to compute the energy balance and two-stream radiative transfer to iterate the model. The TES and MARCI retrieved optical depths are over narrower spectral bands. This means that what is being compared is not necessarily "the same". This leads us to the question: What would TES and MARCI "see" if they were measuring the Mars output from the GCM?

For this meeting we will present preliminary results from doing this type of analysis. From our above three model runs we will use the extracted M_0 and N_0 values and create synthetic MARCI-TES results and compare those to the actual observations.

References

Clancy, R. T., Grossman, A. W., Wolff, M. J., James, P. B., Rudy, D. J., Billawala, Y. N., Sandor, B. J., Lee, S. W., Muhleman, D. O. (1996), Water Vapor Saturation at Low Altitudes around Mars Aphelion: A Key to Mars Climate?, *Icarus*, *122*, 36–62.

Haberle, R. M., Montmessin, F., Kahre, M. A., Hollingsworth, J. L., Schaeffer, J., de Brouchoven de Bergeyck, A., Wilson, J. (2010), The Effects of Radiatively Active Water Ice Clouds on the Martian Global Seasonal Water Cycle, In: AAS/Division for Planetary Sciences Meeting Abstracts #42, Volume 42 of *Bulletin of the American Astronomical Society*, pp. 1031.

James, P. B., Bell, J. F., Clancy, R. T., Lee, S. W., Martin, L. J., Wolff, M. J. (1996), Global imaging of Mars by Hubble space telescope during the 1995 opposition, *J. Geophys. Res. 101 (E8)*, 18883–18890.

Kahre, M. A., Haberle, R. M., Hollingsworth, J. L., Montmessin, F., Brecht, A. S., Urata, R., Klassen, D. R., Wolff, M. J. (2017), Updates On Modeling The Water Cycle With The NASA Ames Mars Global Climate Model, In: This meeting.

Montmessin, F., Forget, F., Rannou, P., Cabane, M., Haberle, R. M. (2004), Origin and role of water ice clouds in the Martian water cycle as inferred from a general circulation model, *J. Geophys. Res. Plan. 109 (E18)*, E10004.

Pearl, J. C., Smith, M. D., Conrath, B. J., Bandfield, J. L., Christensen, P. R. (2001), Observations of Martian ice clouds by the Mars Global Surveyor Thermal Emission Spectrometer: The first Martian year, *J. Geophys. Res.*, *106*, 12325–12338.

Smith, M. D. (2004), Interannual variability in TES atmospheric observations of Mars during 1999-2003, *Icarus*, *167*, 148–165.

Smith, M. D., Bandfield, J. L., Christensen, P. R., Richardson, M. I. (2003), Thermal Emission Imaging System (THEMIS) infrared observations of atmospheric dust and water ice cloud optical depth, *J. Geophys. Res. Plan.*, *108*, 1–1.

Wolff, M. J., Clancy, R. T., Whitney, B. A., Christensen, P. R., Pearl, J. C. (1999), Some Characteristics of the Martian Aphelion Global Cloud Belt, In: The Fifth International Conference on Mars, July 19-24, 1999, Pasadena, California, pp. 6173.